RSC Advances

PAPER

View Article Online
View Journal | View Issue

Cite this: *RSC Adv.*, 2024, **14**, 36902

Synthesis, crystal structure, and antiviral evaluation of new imidazopyridine-schiff base derivatives: *in vitro* and *in silico* anti-HIV studies†

Mohamed Azzouzi, *[a] Abderrahim Ait Ouchaoui,[bc] Omar Azougagh, [a] Salah Eddine El Hadad,[d] Mohamed Abou-salama, [a] Adyl Oussaid,[a] Christophe Pannecouque [e] and Taoufik Rohand *[a]

A series of Imidazo[1,2-*a*]pyridine-Schiff base derivatives were synthesized and characterized using ^{1}H NMR, ^{13}C NMR, Mass Spectrometry and FTIR techniques, and the structure of **4a** was further confirmed through single-crystal X-ray diffraction analysis. Density Functional Theory (DFT) has been used to investigate the structural and electronic properties. The synthesized compounds were evaluated *in vitro* for their antiviral activity against human immunodeficiency virus type-1 (HIV-1) and human immunodeficiency virus type-2 (HIV-2) in MT-4 cells. Compound **4a** displayed EC_{50} values of 82,02 and 47,72 μg ml^{-1} against HIV-1 and HIV-2, respectively. Molecular docking studies were conducted to gain insights into the interaction mechanism of the synthesized compounds with HIV-1 reverse transcriptase. ADME analysis suggested acceptable pharmacokinetic profiles, though solubility remains a limitation for these compounds, highlighting the need for further structural modifications to enhance bioavailability and therapeutic potential.

Received 22nd October 2024
Accepted 13th November 2024

DOI: 10.1039/d4ra07561g

rsc.li/rsc-advances

1. Introduction

Heterocyclic compounds featuring at least one carbon atom and one heteroatom, such as nitrogen or oxygen, are of enormous significance in diverse biological processes. [1] With their unique pharmacological properties and structural adaptability, they have emerged as pivotal components in developing innovative therapeutics.[2] These heterocycles have risen to prominence as essential building blocks due to the unique characteristics and biological activities resulting from incorporating nitrogen atoms into their heterocyclic structures.[3,4] Fused heterocyclic compounds with five or six members have garnered considerable attention in medicinal chemistry due to their versatile pharmacological and therapeutic implications.[5] Within the realm of nitrogen-containing heterocycles, the fusion of imidazole and pyridine moieties, particularly in imidazo[1,2-*a*]pyridine derivatives, stands out as one of the most substantial nitrogen-bridged heterocyclic structures in organic compounds, especially in medicinal chemistry.[6–9]

The Imidazo[1,2-*a*]pyridine scaffold acts as a key pharmacophore motif for the identification and optimization of lead structures, owing to its manifold applications, therapeutic attributes, and facile binding with receptors and enzymes, recognized as privileged scaffold due to its well-established biological activities including antifungal,[10,11] antibacterial,[12–17] antiviral,[18–20] anticancer,[21–25] and anti-inflammatory activities,[26,27] establishing the Imidazo[1,2-*a*]pyridine moiety as a focal point in medicinal chemistry.

On the other hand, Schiff bases stand out as versatile pharmacophores, occupying a prominent position within the realm of organic compounds and finding extensive utility in the design and development of a wide array of bioactive lead compounds.[28–30] The imine group within these compounds plays a crucial role by forming hydrogen bonds with the active sites of receptors and enzyme constituents, lending these compounds a unique capability to intervene in cellular processes.[31,32] These compounds showcase a remarkable spectrum of biological activities, spanning from antifungal,[33,34] and antibacterial,[35] to antimalarial,[36] anticancer,[37,38] antiviral,[39] antitubercular,[40] and antidepressant[41] properties. Overall, the integration of imidazo[1,2-*a*]pyridine and Schiff base into a single pharmacophore could offer even more enhanced and interesting properties, paving the way for their use in a variety of fields.

[a]*Laboratory of Molecular Chemistry, Materials and Environment (LCM2E), Department of Chemistry, Multidisciplinary Faculty of Nador, University Mohamed I, Nador 60700, Morocco. E-mail: azzouzi.mohamed@ump.ac.ma; t.rohand@ump.ac.ma*

[b]*Mohammed VI University of Sciences and Health (UM6SS), Casablanca, Morocco*

[c]*Mohammed VI Center for Research and Innovation (CM6), Rabat 10000, Morocco*

[d]*Chemical and Biochemical Sciences-Green Process Engineering, University Mohammed VI Polytechnic, Ben Guerir, Morocco*

[e]*Rega Institute for Medical Research, Laboratory of Virology and Chemotherapy, K.U. Leuven, Leuven, B-3000, Belgium*

† Electronic supplementary information (ESI) available. CCDC 2391520. For ESI and crystallographic data in CIF or other electronic format see DOI: https://doi.org/10.1039/d4ra07561g

Acquired Immunodeficiency Syndrome (AIDS) is a devastating infectious disease that poses a grave threat to human life caused by the human immunodeficiency virus (HIV), which attacks the immune system and weakens the body's ability to fight off infections and diseases.[42] HIV exists in two main genotypes, HIV-1 and HIV-2, with HIV-1 being the primary pathogenic strain responsible for thousands of deaths each year.[43] Although there is currently no cure for AIDS, combination antiretroviral therapy (cART) can control the virus and improve patient longevity and quality of life.[44] Whereas HIV remains latent in the body and cannot be eradicated, necessitating lifelong treatment.[45] Even so, a major problem is that the rapid emergence of drug-resistant variants limits the long-term efficacy of available anti-HIV drugs and remains one of the most important public health challenges worldwide.[46] Hence, an urgent and desirable requirement for the development of innovative and potent anti-HIV entities has been a very active research field in recent years.

To our knowledge, the literature survey reveals there have been no anti-HIV studies conducted on Imidazo[1,2-*a*]pyridine-Schiff base derivatives. Therefore, as a part of our studies on nitrogen bridgehead heterocycles, we report our contribution to testing these moieties' anti-HIV activity against both HIV-1 and HIV-2 strains. The newly synthesized compounds were characterized using ^{1}H NMR, ^{13}C NMR, Mass Spectrometry, FTIR and single-crystal X-ray diffraction techniques. Additionally, electronic properties were estimated using the density functional theory at the B3LYP/6-311++G(d,p) level of theory to identify potential binding sites and predict chemical behavior. Moreover, the target compounds were screened for their antiviral activities in human T-lymphocyte (MT-4) cells infected with either HIV-1 (III_B) or HIV-2 (ROD). Molecular docking was conducted to provide a comprehensive understanding of the mode of inhibition of the target compounds. Furthermore, drug-likeness and ADME examinations were performed and discussed.

2. Experimental methods

2.1. General information

Chemicals and solvents were reagent grade purchased from commercial suppliers and used as received with no further purification. The NMR spectra were gathered in Chloroform-*D* using the JNM-ECZ500R/S1 FT NMR SYSTEM (JEOL), operating at 500 MHz and 126 MHz for ^{1}H and ^{13}C, respectively. The following abbreviations were used to describe the multiplicity: s = singlet, d = doublet, t = triplet, m = multiplet, dd = doublet of doublets, ddd = doublet of doublets of doublets, td = triplet of doublets, tt = triplet of triplets and the coupling constants (*J*), were reported in the Hertz unit (Hz). Thermo Scientific TSQ 8000 Evo Triple Quadrupole GC-MS/MS spectrometry was employed to acquire the mass spectra. The FT-IR spectra were recorded across the range of 4000–400 cm^{-1} using JASCO FT/IR-4700 spectrophotometers. X-ray diffraction data were obtained from a shock-cooled single crystal at 150 K using a Bruker Venture Metaljet κ-geometry diffractometer. The diffractometer incorporated a Metal Jet with Helios MX Mirror Optics as a monochromator and a Bruker CMOS Photon III detector. Data collection involved the use of an Oxford Cryostream 700 low-temperature device with GaK_{α} radiation (λ = 1.34139 Å). All collected data underwent integration through SAINT, and SADABS applied a multi-scan absorption correction. Structure determination employed intrinsic phasing methods with XT, followed by refinement through full-matrix least-squares against F^2 using XL within the graphical user interface of OLEX2. Anisotropic displacement parameters were assigned to all non-hydrogen atoms, while hydrogen atom positions were determined from a difference Fourier map and refined isotropically.

2.2. Synthesis and crystal growth

The synthetic route leading to the target compounds **4a-d** is depicted in Scheme 1. Initially, 5-chloropyridin-2-amine (**1**, 50 mmol) and phenacyl bromide (50 mmol) were subjected to stirring under solvent-free conditions at 80 °C for 1 h. The resulting precipitate was isolated *via* filtration and subsequently washed with acetone, affording 6-chloro-2-phenylimidazo[1,2-*a*] pyridine (**2**). The 3-amine derivative was synthesized *via* direct nitrosation, where a saturated solution of $NaNO_2$ was added to compound **2** (50 mmol) in AcOH (50 ml) and stirred for 3 hours, yielding a green residue, followed by a reduction treatment involving the addition of a mixture of Zinc powder (2 eq) in

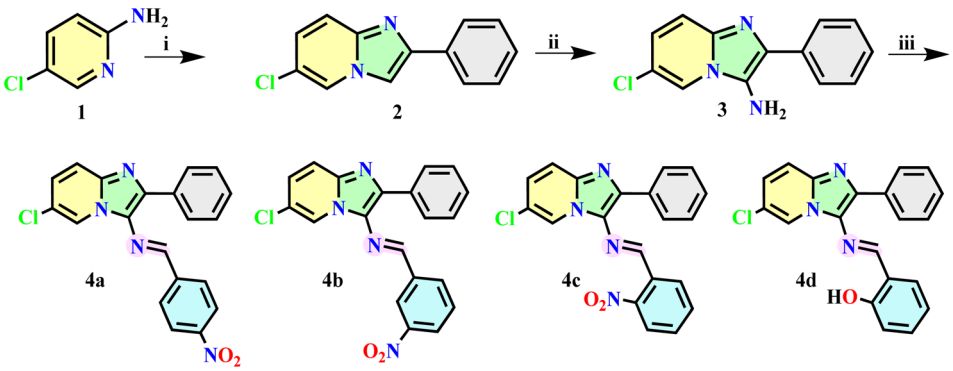

Scheme 1 The synthetic route of target compounds. Reagents and Conditions: (i) phenacyl bromide, solvent-free, 80 °C, 1 h; (ii) $NaNO_2$, AcOH, rt, 3 h, then Zn Powder, AcOH, EtOH, overnight, rt; (iii) substituted aromatic aldehyde, AcOH, EtOH, rt, 24 h.

EtOH (50 ml). The reaction mixture was stirred overnight at room temperature. The resulting solution was filtered, and the pH was adjusted to 9, leading to the precipitation of 6-chloro-2-phenylimidazo[1,2-*a*]pyridin-3-amine (**3**), which was subsequently recrystallized from absolute ethanol to obtain a sufficiently pure product. Subsequently, compound **3** (10 mmol) was condensed with Substituted aromatic aldehydes (10 mmol) in EtOH (50 ml), along with two drops of AcOH as a catalyst. The reaction mixture was stirred at room temperature for 24 hours, resulting in the formation of the corresponding compounds. To ensure high purity for subsequent analyses, recrystallization from absolute ethanol afforded analytically pure products.

A single crystal appropriate for X-ray diffraction examination was generated *via* a mixed-solvent crystallization approach. A concentrated solution of **4a** was produced in a methanol/dichloromethane mixture and subsequently filtered. After five days of evaporation at room temperature, suitable red crystals were obtained for further structural investigation.

2.3. Computational details

To establish a comprehensive link between the structure and its associated behaviors of the investigated compounds, the DFT method at the B3LYP/6-311++G(d,p) basis set was employed within the Gaussian 09 suite. Utilizing Gauss View 6 software, Frontier Molecular Orbitals (FMOs), and key reactivity descriptors, as well as Molecular Electrostatic Potential (MEP) Surface and Mulliken atomic charge were computed and visually represented to identify potential binding sites. Additionally, Electron Localization Function (ELF), Localized Orbital Locator (LOL) and Quantum Theory of Atoms in Molecule (QTAIM) analysis were conducted and visually represented using the Multiwfn code, VMD and Gnuplot tools.[47]

2.4. *In vitro* anti-HIV assay in MT-4 cells

In vitro anti-HIV assay evaluation of the antiviral activity of compounds **4a–e** against HIV-1 (III_B) and HIV-2 (ROD) strains in MT-4 cells was performed using the 3-(4,5-dimethylthiazol-2-yl)-2,5-diphenyltetrazolium bromide (MTT) method as described by Pannecouque*et al.*, 2008.[48] In brief, stock solutions (10 times the final concentration) of the test compounds were added in 25 μl volumes to two series of triplicate wells to simultaneously assess their effects on mock and HIV-infected cells at the start of each experiment. Serial 5-fold dilutions of test compounds were made directly in flat-bottomed 96-well microtiter trays using a Biomek 3000 robot (Beckman instruments). Untreated HIV- and mock-infected cell samples were included as controls for each sample. HIV-1 (III_B) or HIV-2 (ROD) stock (50 μl) at 100–300 $CCID_{50}$ (50% cell culture infectious dose) or culture medium [10% heat-inactivated Fetal Calf Serum (FCS), 2 mM-glutamine, 0.1% sodium bicarbonate, and 20 μg ml^{-1} gentamicin] was added to either of the infected or mock-infected wells of the microtiter tray. Mock-infected cells were used to evaluate the effect of the test compound on uninfected cells in order to assess the cytotoxicity of the test compounds. Exponentially growing MT-4 cells were centrifuged for 5 min at 1000 rpm and the supernatant was discarded. The MT-4 cells were resuspended at 6 $\times 10^5$ cells per mL, and 50 μL volumes were transferred to the microtiter tray wells. Five days after infection, the viability of mock- and HIV-infected cells was examined spectrophotometrically by the MTT method.

2.5. Molecular docking analysis

2.5.1. Protein preparation. The docking studies were conducted on HIV-1 Reverse Transcriptase (PDB ID: 1REV). The crystal structures of this key protein were obtained from the Protein Data Bank (PDB)[49] and prepared for docking using AutoDock Tools.[50] The preparation process involved the removal of all water molecules and co-crystallized ligands, the addition of polar hydrogens, and the assignment of Kollman. The grid box was centered at coordinates $X = 3.678$, $Y = -40.856$, $Z = 23.497$, with a box size of 23 × 23 × 23 Å. These parameters were selected to encompass the active sites of the protein, ensuring adequate coverage of the binding pockets during the docking process.

2.5.2. Ligand preparation. The synthesized compounds were not available in public databases such as PubChem due to their novel nature. Consequently, the three-dimensional structures of these compounds were obtained from CIF (Crystallographic Information File) format and optimized using the DFT method with the B3LYP/6-311++G(d,p) basis set, which was converted to PDB format using OpenBabel.[51] The PDB files were then prepared for docking by optimizing the geometry, adding necessary hydrogens, and assigning Gasteiger charges and saved in PDBQT format. Along with the synthesized compounds, two control molecules, Nevirapine and Didanosine, were included in the study as control compounds. The SDF files for these reference ligands were retrieved from PubChem[52] and then converted to PDB by OpenBabel and similarly prepared using the same protocol as for the synthesized compounds.

2.5.3. Docking procedure and molecular interactions analysis. Docking simulations were performed using AutoDock Vina.[53] For each protein–ligand pair, the docking was conducted within the predefined grid box parameters to explore potential binding modes of the synthesized compounds and control molecules. The exhaustiveness of the search was set to 8 to ensure a comprehensive exploration of the binding conformations. The results were ranked based on binding affinity, with the lowest energy (kcal mol^{-1}).

The visualization of 2D interactions and 3D binding poses between the synthesized compounds and target proteins was conducted using BIOVIA Discovery Studio.[54] Docking results from AutoDock Vina, comprising protein–ligand complexes for HIV-1 Reverse Transcriptase (PDB ID: 1REV), were imported into the software. Interaction analyses were focused on residues within a 5 Å radius of the ligand, capturing key interactions such as hydrogen bonds, hydrophobic interactions, and electrostatic contacts.

2.6. ADME profiling

The ADME properties of the Four synthesized compounds and two reference molecules, Nevirapine and Didanosine, were

evaluated using the SwissADME web tool,[55] with a specific focus on solubility. The molecular structures were prepared in PDB format and converted to SMILES format for input into SwissADME. The analysis predicted key pharmacokinetic parameters, including lipophilicity (XlogP3), water solubility (Log *S*), solubility class, gastrointestinal (GI) absorption, blood–brain barrier (BBB) permeability, P-glycoprotein (Pgp) substrate status, cytochrome P450 inhibition (CYP2D6 and CYP3A4), and PAINS alerts. Particular attention was given to solubility parameters to assess the potential bioavailability and effectiveness of the compounds in biological environments.

3. Results and discussion

3.1. Chemistry

In this study, novel Schiff base heterocycles derived from imidazo[1,2-*a*]pyridine have been synthesized using easy and conventional methods according to the literature procedure. Initially, 6-chloro-2-phenylimidazo[1,2-*a*]pyridine (**2**) was obtained by the condensation of commercially available 5-chloropyridin-2-amine (**1**) with Phenacyl bromide. Subsequently, the intermediate (**2**) was functionalized at the C-3 position by introducing an NO group and subsequently reduced to NH_2 under the conditions of $NaNO_2$/AcOH and Zn/AcOH/EtOH respectively, resulting in the formation of the 3-amino product, 6-chloro-2-phenylimidazo[1,2-*a*]pyridin-3-amine (**3**), which subjected to reaction with substituted aromatic aldehydes, leading to the synthesis of the target compounds **4a–d**.

The structural assignments of all newly synthesized imines were validated through comprehensive analytical and spectral analyses. The ^{1}H NMR spectra of compounds **4a–d** exhibited the expected characteristic signals, notably a singlet observed at δ 8.73–9.23 ppm, attributable to the proton of the imine group (N=CH). Additionally, in the ^{13}C NMR spectra, a prominent peak emerged at δ 150.16–163.91 ppm, attributable to the carbon (N=CH) of the imine moiety. The IR spectra of **4a–d** provided additional confirmation, showing an absorption band around 1597–1703 cm^{-1}, which is suggestive of the (C=N) stretching vibration. Moreover, LC-MS analysis further confirmed the molecular weights of the compounds, thereby supporting the fact that the expected Schiff base heterocyclic derivatives have indeed been successfully formed (ESI file†).

3.1.1 (*E*)-6-Chloro-*N*-(4-nitrobenzylidene)-2-phenylimidazo[1,2-*a*]pyridin-3-amine (4a). Yield 94%. Mp; 218–220 °C, ^{1}H NMR (500 MHz, Chloroform-*D*) δ 8.81 (s, 1H), 8.50 (dd, J = 2.1, 0.9 Hz, 1H), 8.27 (d, J = 8.8 Hz, 2H), 7.92 (d, J = 8.8 Hz, 2H), 7.74 (dd, J = 8.3, 1.5 Hz, 2H), 7.54 (dd, J = 9.4, 0.9 Hz, 1H), 7.51–7.42 (m, 2H), 7.41 (tt, J = 7.3, 1.5 Hz, 1H), 7.25 (dd, J = 9.4, 2.1 Hz, 1H). ^{13}C NMR (126 MHz, Chloroform-*D*) δ 152.56, 149.09, 142.09, 141.88, 136.95, 134.20, 129.21, 128.97, 128.81, 128.57, 128.29, 127.48, 124.20, 121.59, 121.49, 118.11. FT-IR: ν(C–H) = 3068, 3004 cm^{-1}; ν(C=N) = 1597 cm^{-1}; ν(C=C) = 1569 cm^{-1}; ν(N=O) = 1507, 1326 cm^{-1}; ν(C–N) = 1230 cm^{-1}; ν(C–C) = 1103 cm^{-1}; ν(C–Cl) = 792 cm^{-1}. LC-MS: m/z = 377.079 (M + 1).

3.1.2 (*E*)-6-Chloro-*N*-(3-nitrobenzylidene)-2-phenylimidazo[1,2-*a*]pyridin-3-amine (4b). Yield 86%. Mp; 211–213 °C, ^{1}H NMR (500 MHz, Chloroform-*D*) δ 8.80 (s, 1H), 8.59 (t, J = 2.0 Hz, 1H), 8.50 (dd, J = 2.0, 0.9 Hz, 1H), 8.28 (ddd, J = 7.9, 2.0, 1.3 Hz, 1H), 8.11 (ddd, J = 7.9, 1.9, 1.3 Hz, 1H), 7.74 (dd, J = 8.6, 1.5 Hz, 2H), 7.62 (t, J = 7.9 Hz, 1H), 7.54 (dd, J = 9.5, 0.8 Hz, 1H), 7.46 (dd, J = 8.6, 7.2 Hz, 2H), 7.41 (tt, J = 7.2, 1.5 Hz, 1H), 7.24 (dd, J = 9.5, 2.0 Hz, 1H). ^{13}C NMR (126 MHz, Chloroform-*D*) δ 153.29, 148.86, 141.84, 138.03, 136.37, 134.19, 133.64, 129.97, 129.23, 128.88, 128.50, 128.20, 127.24, 125.55, 122.84, 121.46, 121.43, 118.04. FT-IR: ν(C–H) = 3127, 3063 cm^{-1}; ν(C=N) = 1613 cm^{-1}; ν(C=C) = 1568 cm^{-1}; ν(N=O) = 1524, 1332 cm^{-1}; ν(C–N) = 1228 cm^{-1}; ν(C–C) = 1073 cm^{-1}; ν(C–Cl) = 774 cm^{-1}. LC-MS: m/z = 377.079 (M + 1).

3.1.3 (*E*)-6-Chloro-*N*-(2-nitrobenzylidene)-2-phenylimidazo[1,2-*a*]pyridin-3-amine (4c). Yield 89%. Mp; 220–222 °C, ^{1}H NMR (500 MHz, Chloroform-*D*) δ 9.23 (s, 1H), 8.53 (dd, J = 2.0, 1.1 Hz, 1H), 8.34 (dd, J = 7.9, 1.5 Hz, 1H), 7.98 (dd, J = 8.2, 1.2 Hz, 1H), 7.77 (dd, J = 8.3, 1.4 Hz, 2H), 7.73 (ddd, J = 7.9, 7.3, 1.2 Hz, 1H), 7.60 (dd, J = 9.5, 1.1 Hz, 1H), 7.57 (ddd, J = 8.2, 7.3, 1.5 Hz, 1H), 7.49 (dd, J = 8.3, 7.3 Hz, 2H), 7.42 (tt, J = 7.3, 1.4 Hz, 1H), 7.27 (dd, J = 9.5, 2.0 Hz, 1H). ^{13}C NMR (126 MHz, Chloroform-*D*) δ 150.16, 149.13, 141.78, 133.53, 133.33, 131.17, 131.02, 129.20, 129.09, 129.06, 128.72, 128.23, 127.53, 124.84, 121.63, 121.56, 118.01. FT-IR: ν(C–H) = 3079, 3024 cm^{-1}; ν(C=

Table 1 Crystallographic Data and Refinement Parameters for **4a**

Parameter	Values
Empirical formula	$C_{20}H_{13}ClN_4O_2$
Formula weight	376.79
Temperature [K]	150
Crystal system	Monoclinic
Space group (number)	$P2_1/c$ (14)
a [Å]	10.7755(6)
b [Å]	26.7963(15)
c [Å]	12.0718(6)
α [°]	90
β [°]	102.178(3)
γ [°]	90
Volume [Å^3]	3407.2(3)
Z	8
ρ_{calc} [g cm^{-3}]	1.469
μ [mm^{-1}]	1.441
F(000)	1552
Crystal size [mm^3]	0.04 × 0.13 × 0.13
Crystal colour	Clear light red
Crystal shape	Plate
Radiation	GaK_α (λ = 1.34139 Å)
2θ range [°]	7.12 to 158.31 (0.68 Å)
Index ranges	$-15 \le h \le 15$
	$-39 \le k \le 39$
	$-17 \le l \le 15$
Reflections collected	114 388
Independent reflections	11 104
	R_{int} = 0.0493
	R_{sigma} = 0.0248
Completeness to θ = 53.594°	100.0%
Data/restraints/parameters	11 104/0/591
Goodness-of-fit on F^2	1.064
Final R indexes [$I \ge 2\sigma(I)$]	R_1 = 0.0407 wR_2 = 0.1019
Final R indexes [all data]	R_1 = 0.0508 wR_2 = 0.1088
Largest peak/hole [e Å^{-3}]	0.28/−0.39

C) = 1562 cm^{-1}; ν(N=O) = 1513, 1330 cm^{-1}; ν(C–N) = 1222 cm^{-1}; ν(C–C) = 1092 cm^{-1}; ν(C–Cl) = 806 cm^{-1}. LC-MS: *m*/*z* = 377.079 (M + 1).

3.1.4 (*E*)-2-(((6-chloro-2-phenylimidazo[1,2-*a*]pyridin-3-yl) imino)methyl)phenol (4d). Yield 83%. Mp; 130–132 °C, ^{1}H NMR (500 MHz, Chloroform-*D*) δ 12.33 (s, 1H), 8.73 (s, 1H), 8.20 (dd, *J* = 2.0, 0.8 Hz, 1H), 7.75 (dd, *J* = 8.4, 1.4 Hz, 2H), 7.65 (dd, *J* = 9.5, 0.8 Hz, 1H), 7.43 (dd, *J* = 8.5, 7.4 Hz, 2H), 7.40–7.37 (m, 1H), 7.36 (tt, *J* = 7.4, 1.4 Hz, 1H), 7.22 (dd, *J* = 9.5, 2.0 Hz, 1H), 7.09 (dd, *J* = 7.6, 1.7 Hz, 1H), 7.05 (dd, *J* = 8.4, 1.2 Hz, 1H), 6.90 (td, *J* = 7.6, 1.2 Hz, 1H). ^{13}C NMR (126 MHz, Chloroform-*D*) δ 176.12, 163.91, 160.86, 141.10, 134.80, 134.10, 133.21, 132.69, 129.25, 128.68, 128.22, 127.00, 121.85, 120.24, 119.84, 119.03, 118.12, 117.43. FT-IR: ν(O–H) = 3393 cm^{-1}; ν(C–H) = 3078, 3024 cm^{-1}; ν(C=N) = 1703 cm^{-1}; ν(C=C) = 1623 cm^{-1}; ν(C–O) = 1444 cm^{-1}; ν(C–N) = 1267 cm^{-1}; ν(C–Cl) = 751 cm^{-1}. LC-MS: *m*/*z* = 349.092 (M + 1).

3.2. Single crystal XRD studies

Given the importance of molecular structure and conformation in dictating biological activities, particularly in interactions with enzyme or receptor active sites, compound **4a** was subjected to single crystal X-ray diffraction analysis. This approach aims to provide a comprehensive and definitive validation of the structural assignment of these compounds.

The grown crystal of **4a** was subjected to single crystal X-ray diffraction studies, solved and refined. Table 1 shows a detailed report of the structure refinement. The compound **4a** crystallizes in the monoclinic system with the space group $P2_1/c$ with eight molecules in a unit cell. The unit cell dimensions observed are *a* = 10.7755(6) A°, *b* = 26.7963(15) A°, *c* = 12.0718(6) A°, $\alpha = 90°$, $\beta = 102.178(3)°$, $\gamma = 90°$. Fig. 1 depicts the molecular structure of **4a** using 50% probability thermal displacement ellipsoids, with hydrogen atoms depicted as spheres of arbitrary size for clarity. The figure provides a separate view of the two molecules of the asymmetric unit, along with the atomic numbering scheme. Fig. 2 displays a view of the two molecules of the asymmetric unit within the unit cell. The adjacent molecules are interconnected through hydrogen bonding interactions of C–H···N and C–H···O types (Table 2), resulting in the formation of a dimer, as depicted in Fig. 3. The imidazopyridine ring of the molecules in the dimer forms dihedral angles of 34.29° and 27.87° with the phenyl plane (C8A–C13A) and (C8B–C13B), respectively. In molecule B, the phenyl group (C15B–C20B) is nearly planar with the imidazopyridine ring (1.70°), while in molecule A, it forms a dihedral angle of 73.40°. The configuration of the C=N bond in the imine is described as "anti" to reduce overall steric hindrance. The crystal lattice reveals that the molecules are stacked in the form of parallel packs along the *c*-axis direction (Fig. 3). In Table 3, selected bond distances and bond angles of compound **4a** have been presented.

3.3. Density functional theory (DFT) calculations

3.3.1. Geometry and frontier molecular orbitals (FMOs) investigations. The utilization of DFT in quantum chemical computations offers significant advantages in discerning optimal molecular structures and predicting diverse properties, encompassing total energy and electronic structure to establish a connection between the molecular structure under investigation and their associated behaviors. Molecular structure optimization of **4a-d** was conducted to identify the most stable

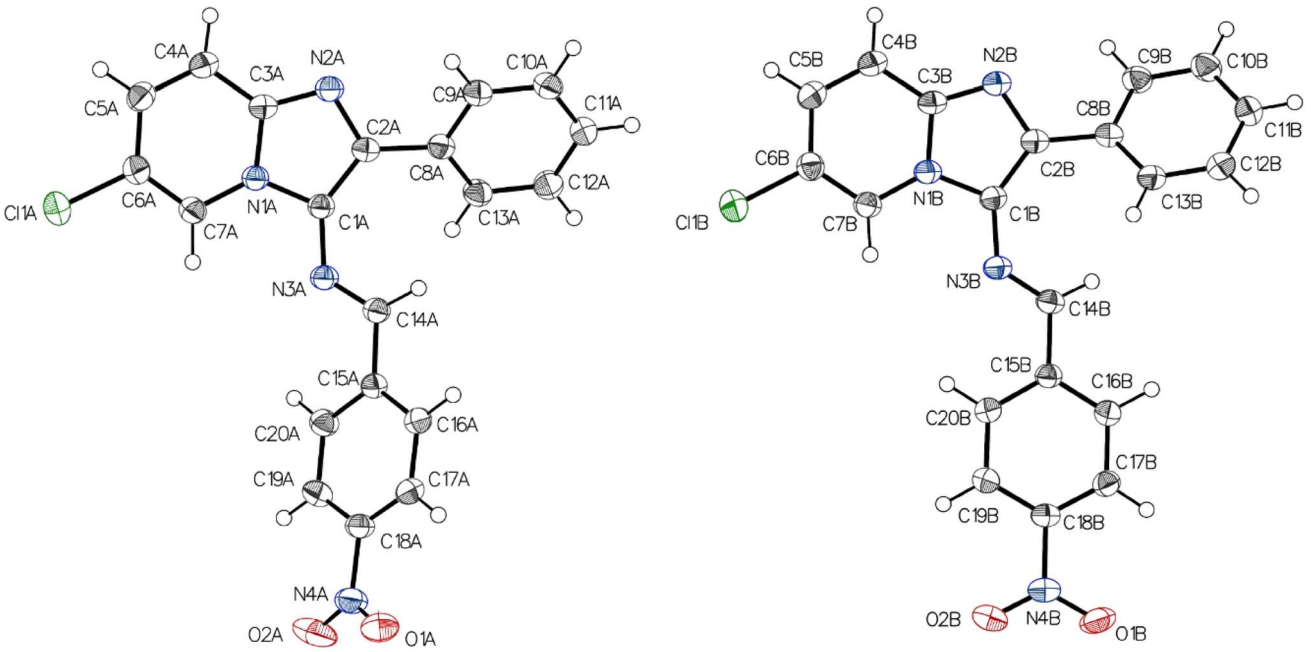

Fig. 1 The molecular structure of **4a**, showing the atom-numbering scheme. Ellipsoids are drawn at the 50% probability level, and hydrogen atoms are shown as spheres of arbitrary size.

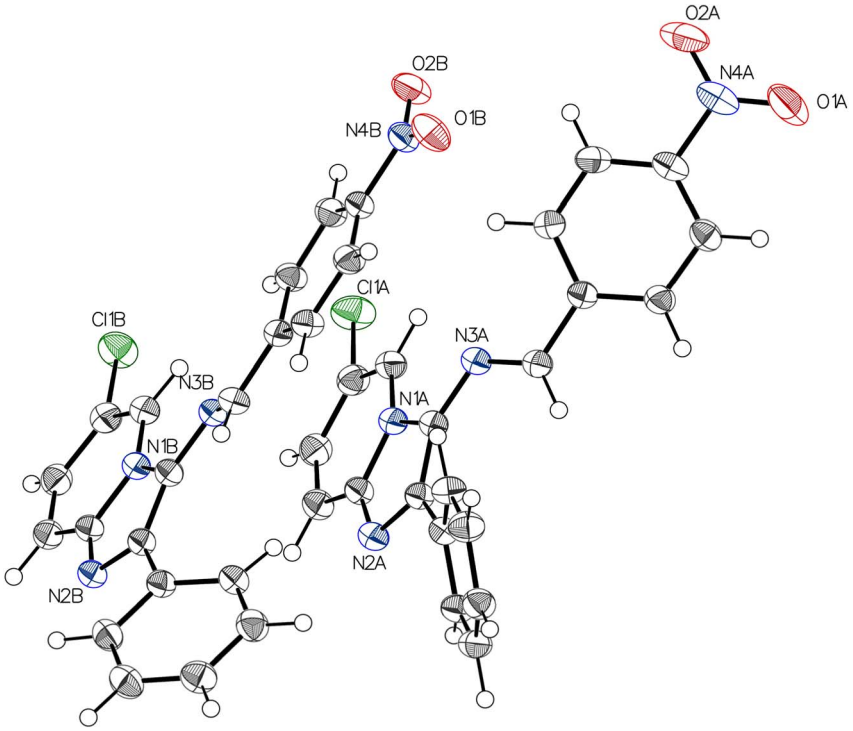

Fig. 2 ORTEP representation of the dimer of two molecular units of **4a**. Ellipsoids are drawn at the 50% probability level, and hydrogen atoms are shown as spheres of arbitrary size.

Table 2 Hydrogen bonds for **4a**

D–H···A	D–H	H···A	D···A	DHA
C4A–H4A···N2B[a]	0.970(16)	2.445(16)	3.4088(14)	172.7(14)
C14A–H14A···O1B[b]	0.982(16)	2.604(16)	3.5192(15)	155.0(12)
C4B–H4B···N2A[a]	0.971(16)	2.669(17)	3.6324(14)	171.6(14)

[a] Symmetry transformations used to generate equivalent atoms: $1-X$, $1-Y$, $-Z$. [b] $+X$, $0.5-Y$, $-0.5+Z$.

ground state geometry for each molecule. Subsequently, vibrational frequency calculations were executed to validate the absence of negative or imaginary frequencies, thereby affirming the optimized geometry as representing an energy minimum configuration.[56] Consequently, the stable configurations were successfully determined and are illustrated in Fig. 4.

Frontier Molecular Orbitals (FMOs) are a key concept in theoretical chemistry, particularly in the field of organic chemistry.[57] They play a crucial role in understanding and predicting the reactivity of organic molecules. Central to FMO analysis are the Highest Occupied Molecular Orbital (HOMO) and the Lowest Unoccupied Molecular Orbital (LUMO), often referred to as the "frontier" orbitals due to their decisive roles in chemical interactions. The HOMO signifies the electron-donating capacity of a molecule, while the LUMO represents its electron-accepting capacity. The energy difference between these orbitals, known as the HOMO–LUMO gap (ΔE_{gap}), serves as a critical parameter governing the molecule's reactivity and stability. A small ΔE_{gap} suggests heightened reactivity, whereas a wider gap implies diminished reactivity and increased stability. This concept holds particular significance in biological systems, where ΔE_{gap} determines a molecule's propensity to engage in chemical interactions, such as binding to proteins or enzymes. Consequently, a profound understanding of FMOs and the HOMO–LUMO gap is indispensable for forecasting the behavior of compounds in biological settings and assessing their potential efficacy as active agents. The graphical illustrations of FMOs for the optimized configurations are presented in Fig. 5. The green and red areas indicate MOs with opposing phases, the positive phase is illustrated in red, while the negative phase is displayed in green. It is evident that the HOMOs are distributed across the entire molecule. Conversely, the LUMOs are typically positioned on the substituted phenyl nuclei.[58–60]

In the investigation of molecular reactivity and electronic structure, FMOs analysis was used to derive the global reactivity descriptors. Table 4 presents a comparative overview of these descriptors, providing valuable insights into the electronic properties and potential reactivity of the studied compounds. Notably, compounds **4a** exhibit smaller ΔE_{gap} values, suggesting heightened reactivity and potential for chemical interactions, whereas compounds **4d** exhibit larger gaps, generally correlating with higher stability and reduced reactivity. Compound **4a** showcases the lowest hardness (1.40 eV) and highest softness (0.72 eV), suggesting a relatively more reactive and responsive to changes in electron density. Furthermore, the electronegativity (χ) and electrophilicity index (ω) values shed light on the molecules' interaction capabilities. Specifically, **4a**

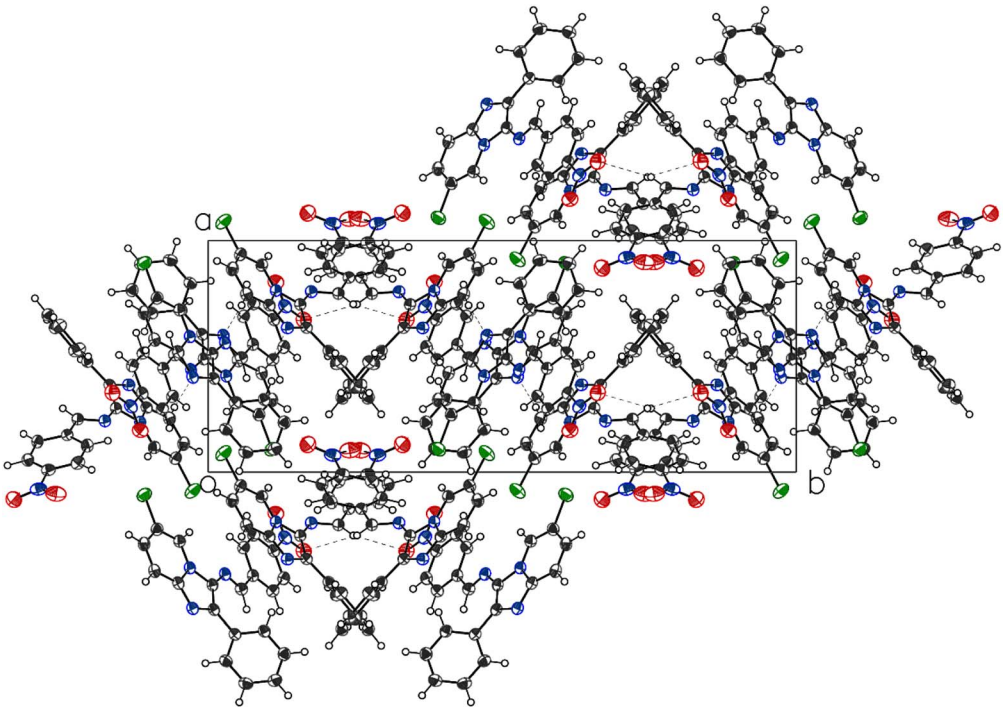

Fig. 3 Molecular packing of the title compound, Projection along the *c*-axis.

Table 3 Some bond distances (Å) and bond angles (°) of **4a**

Bond lengths (Å)					
Cl1A–C6A	1.7349(12)	C16A–C17A	1.3930(15)	O2B–N4B	1.2276(15)
O1A–N4A	1.2238(18)	C17A–H17A	0.962(18)	N2B–C2B	1.3681(14)
N1A–C1A	1.3912(14)	C17A–C18A	1.3867(17)	N2B–C3B	1.3339(15)
N1A–C3A	1.3890(13)	C18A–C19A	1.3836(19)	C2B–C8B	1.4704(16)
N1A–C7A	1.3760(14)	C19A–H19A	0.946(17)	N3B–C14B	1.2812(15)
C1A–C2A	1.3997(14)	C19A–C20A	1.3846(16)	C3B–C4B	1.4113(16)
C1A–N3A	1.3796(13)	C20A–H20A	0.964(16)	N4B–C18B	1.4707(13)
O2A–N4A	1.2295(17)	Cl1B–C6B	1.7353(12)	C4B–H4B	0.971(16)
N2A–C2A	1.3712(14)	O1B–N4B	1.2253(15)	C4B–C5B	1.3690(17)
N2A–C3A	1.3328(15)	N1B–C1B	1.3948(14)	C5B–H5B	0.942(18)
C2A–C8A	1.4698(16)	N1B–C3B	1.3863(13)	C5B–C6B	1.4209(16)
N3A–C14A	1.2821(15)	N1B–C7B	1.3702(15)	C6B–C7B	1.3568(17)
C3A–C4A	1.4134(16)	C1B–C2B	1.4068(14)	C7B–H7B	0.989(15)
N4A–C18A	1.4690(14)	C1B–N3B	1.3738(13)	C8B–C9B	1.4001(15)
Bond angles (°)					
C3A–N1A–C1A	107.18(9)	N1A–C7A–H7A	116.8(9)	C3B–N2B–C2B	106.46(9)
C7A–N1A–C1A	129.44(9)	C6A–C7A–N1A	117.27(10)	C1B–C2B–C8B	130.84(10)
C7A–N1A–C3A	123.06(10)	C6A–C7A–H7A	126.0(9)	N2B–C2B–C1B	110.55(10)
N1A–C1A–C2A	104.81(9)	C9A–C8A–C2A	118.83(10)	N2B–C2B–C8B	118.48(9)
N3A–C1A–N1A	115.79(9)	C13A–C8A–C2A	122.41(10)	C14B–N3B–C1B	124.36(10)
N3A–C1A–C2A	139.33(11)	C13A–C8A–C9A	118.65(11)	N1B–C3B–C4B	118.82(10)
C3A–N2A–C2A	106.02(9)	C8A–C9A–H9A	117.9(9)	N2B–C3B–N1B	110.95(9)
C1A–C2A–C8A	130.26(10)	C3B–N1B–C1B	107.34(9)	N2B–C3B–C4B	130.24(10)
N2A–C2A–C1A	110.86(10)	C7B–N1B–C1B	129.51(9)	O1B–N4B–O2B	123.62(10)
N2A–C2A–C8A	118.85(9)	C7B–N1B–C3B	123.14(10)	O1B–N4B–C18B	118.19(10)
C14A–N3A–C1A	122.62(10)	N1B–C1B–C2B	104.64(9)	O2B–N4B–C18B	118.19(10)
N1A–C3A–C4A	118.76(10)	N3B–C1B–N1B	115.35(9)	C3B–C4B–H4B	119.7(10)
N2A–C3A–N1A	111.09(9)	N3B–C1B–C2B	139.92(11)	C5B–C4B–C3B	119.01(10)
N2A–C3A–C4A	130.12(10)	C3B–N1B–C1B	107.34(9)	C5B–C4B–H4B	121.3(10)

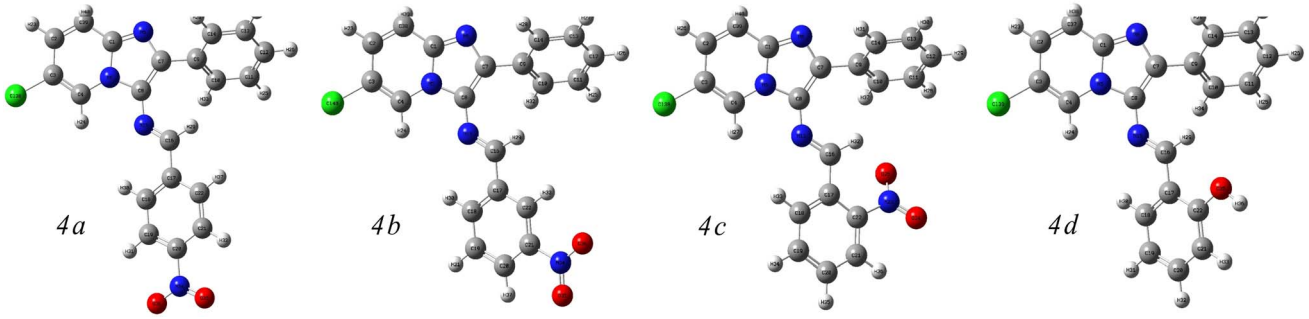

Fig. 4 The optimized molecular structures of **4a-d**.

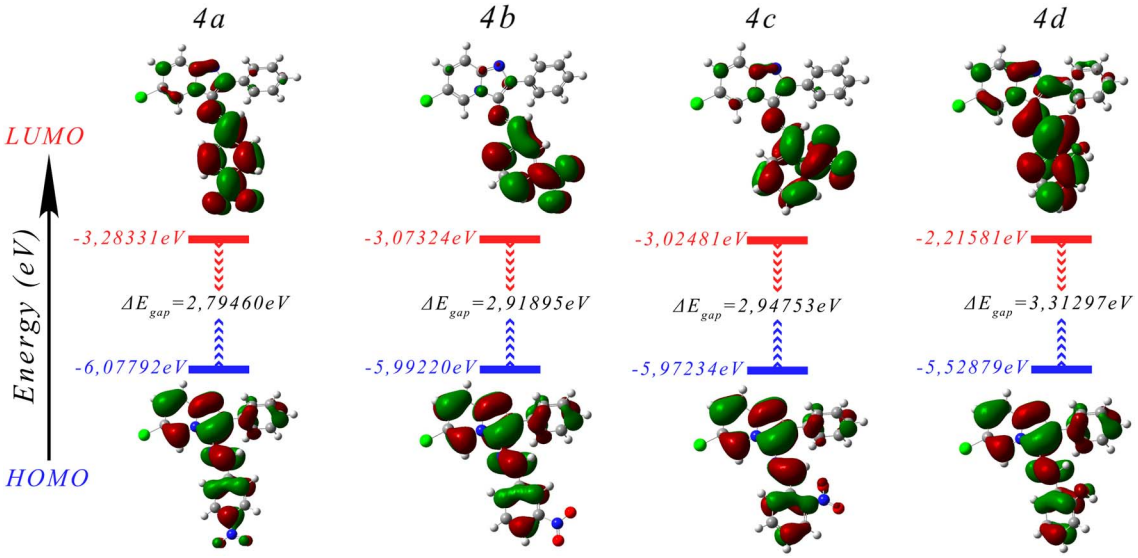

Fig. 5 Correlation diagram between HOMO and LUMO of **4a–d**.

demonstrates the highest χ (4.68061 eV) and ω (7.83946 eV) values, suggesting its enhanced ability to engage in electron transfer processes and interact with receptors, which could be beneficial for biological applications. Overall, the variations in these descriptors among the compounds underscore their distinct reactivity and stability profiles.[59–66]

3.3.2. Molecular electrostatic potential (MEP) analysis. Molecular electrostatic potential (MEP) analysis is a fundamental tool in computational chemistry used to visualize and understand the distribution of electron density within a molecule. MEP offers a valuable understanding of the electrostatic interactions that occur during chemical reactions, binding processes, and molecular recognition events.[67] By mapping the MEP onto the molecular surface and utilizing a color spectrum to differentiate various electrostatic potential energy levels, regions of positive and negative electrostatic potential can be identified. Positive regions indicate areas characterized by electron deficiency or electrophilic nature, depicted in blue, while negative regions represent areas with electron-rich or nucleophilic character shown in red. These electrostatic features play a crucial role in molecular recognition, such as ligand binding to receptors or enzymes, and can provide valuable information for drug design and molecular docking studies.[68]

Table 4 Global reactivity descriptors of **4a–d**

Quantum parameters	4a	4b	4c	4d
E_{HOMO} (eV)	−6.07792	−5.99220	−5.97234	−5.52879
E_{LUMO} (eV)	−3.28331	−3.07324	−3.02481	−2.21581
ΔE_{gap} (eV)	2.79460	2.91895	2.94753	3.31297
η (eV)	1.39730	1.45947	1.47376	1.65648
σ (eV^{-1})	0.71566	0.68517	0.67853	0.60368
χ (eV)	4.68061	4.53272	4.49857	3.87230
ω (eV)	7.83946	7.03867	6.86581	4.52606

The MEP maps generated at the optimized geometries are depicted in Fig. 6. In **4a–d**, the areas surrounding the nitrogen atom N-6 of the imidazole moiety, in conjunction with the NO_2 groups, exhibit pronounced electron-rich characteristics, indicating a strong affinity for electrophiles. Consequently, these regions are expected to serve as sites for nucleophilic attack. Conversely, regions of electron deficiency are observed around

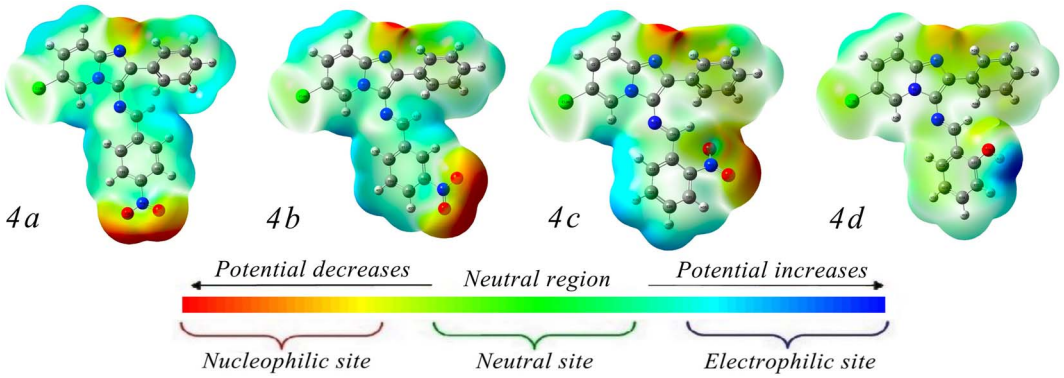

Fig. 6 MEP surface of **4a–d**.

the hydrogen atoms, notably around the hydrogen of the OH group in **7d**. These regions signify electrophilic sites capable of attracting nucleophilic entities. MEP analysis is particularly useful for predicting sites of electrophilic or nucleophilic attack, identifying potential binding sites for substrates or inhibitors, and understanding the reactivity and selectivity of chemical reactions.

3.3.3. Mulliken charge analysis. Mulliken charge analysis is a computational technique used in quantum chemistry to assess the distribution of electron density within a molecule. It involves calculating the partial charges associated with each atom in a molecule based on its electronic structure.[69] Mulliken charges provide valuable insights into the electronegativity and reactivity of individual atoms within a molecular system. These charges can help identify regions of electron accumulation or depletion, aiding in the understanding of chemical bonding, molecular interactions, and reactivity patterns.[70]

The Mulliken atomic charge analysis, as presented in Fig. 7 and Table 5, offers insight into the electron distribution within these compounds. The computed atomic charges, expressed in atomic units (a.u.), reveal the varying degrees of electron density surrounding each atom. Carbon atoms typically exhibit a wide range of charges, reflecting their diverse bonding environments and electronic interactions. The presence of negative charges on C-5 suggests an accumulation of electron density, which may stem from the electron-donating tendencies of neighboring atoms. Notably, carbon atoms directly bonded to electronegative species like nitrogen or oxygen often display more positive charges, indicative of electron withdrawal.[71] Conversely, nitrogen atoms generally show slightly positive charges, suggesting a partial donation of electron density primarily attributed to the involvement in resonance structures. Hydrogen atoms attached to these molecules tend to have positive charges, consistent with their typical behavior as electron donors. Interestingly, the presence of halogen atoms such as chlorine alters the charge distribution, leading to more positively charged neighboring carbon atoms.[72]

3.3.4. ELF and LOL analysis. The analysis conducted using the Electron Localization Function (ELF) and the Localized Orbital Locator (LOL) offers valuable insights into the electron density and bonding characteristics within molecules.[73] In this investigation, color-filled maps representing ELF and LOL were generated through the utilization of the Multiwfn 3.8 program. The ELF color-filled map displayed in Fig. 8 features a color scale bar spanning from 0.000 to 1.000. Regions exhibiting ELF values below 0.500, as depicted by the blue color surface, signify the presence of delocalized electrons surrounding carbon and oxygen atoms. Conversely, regions of pronounced electron localization, particularly in the vicinity of hydrogen atoms, particularly associated with the Imidazopyridine ring, are highlighted in red, indicating elevated ELF values exceeding 0.500.[74]

In contrast, the LOL color-filled map showcased in Fig. 8 reveals smaller LOL values, represented by blue and white regions, primarily observed in valence regions such as those surrounding carbon, nitrogen, and chlorine atoms, suggesting

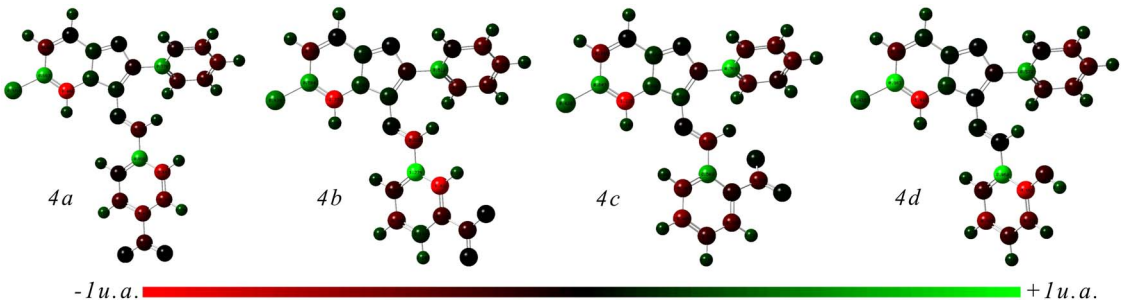

Fig. 7 Optimized structures with Mulliken atomic charges designated by a color change on atoms.

Table 5 The Mulliken atomic charges of **4a–d**

4a		**4b**		**4c**		**4d**	
Atom	Charge(a.u.)	Atom	Charge(a.u.)	Atom	Charge(a.u.)	Atom	Charge(a.u.)
C-1	0.203994	C-1	0.185665	C-1	0.226520	C-1	0.146311
C-2	−0.332893	C-2	−0.299092	C-2	−0.400394	C-2	−0.329245
C-3	0.624179	C-3	0.545881	C-3	0.692295	C-3	0.851660
C-4	−1.374555	C-4	−1.312930	C-4	−1.436671	C-4	−1.772958
N-5	0.153961	N-5	0.159470	N-5	0.172304	N-5	0.161004
N-6	0.038980	N-6	0.032879	N-6	0.040087	N-6	0.030745
C-7	−0.122225	C-7	−0.121464	C-7	−0.189184	C-7	−0.033622
C-8	0.109309	C-8	0.110638	C-8	0.061244	C-8	0.057807
C-9	0.671143	C-9	0.726014	C-9	0.752757	C-9	0.685316
C-10	−0.270178	C-10	−0.307890	C-10	−0.200300	C-10	−0.316664
C-11	−0.272456	C-11	−0.290127	C-11	−0.197174	C-11	−0.304427
C-12	−0.317998	C-12	−0.309185	C-12	−0.302677	C-12	−0.286754
C-13	−0.325595	C-13	−0.334433	C-13	−0.361800	C-13	−0.389736
C-14	−0.121458	C-14	−0.115391	C-14	−0.313337	C-14	−0.039869
N-15	0.035789	N-15	0.024729	N-15	−0.007140	N-15	0.018148
C-16	−0.285280	C-16	−0.624930	C-16	−0.244269	C-16	−0.063480
C-17	0.660660	C-17	1.185587	C-17	0.603634	C-17	0.812139
C-18	−0.080022	C-18	−0.197777	C-18	−0.453849	C-18	−0.233247
C-19	−0.252564	C-19	−0.323868	C-19	−0.486856	C-19	−0.466159
C-20	−0.389093	C-20	0.169558	C-20	−0.201515	C-20	−0.206736
C-21	−0.374148	C-21	−0.186389	C-21	−0.394111	C-21	−0.420447
C-22	−0.641921	C-22	−1.420155	C-22	−0.053781	C-22	−0.793863
H-23	0.197587	H-23	0.197378	N-23	−0.347589	H-23	0.188161
H-24	0.176843	H-24	0.177603	O-24	0.030812	H-24	0.186352
H-25	0.179643	H-25	0.179711	O-25	0.048861	H-25	0.176253
H-26	0.163104	H-26	0.163272	H-26	0.196746	H-26	0.156113
H-27	0.177306	H-27	0.175969	H-27	0.193655	H-27	0.168074
H-28	0.206470	H-28	0.205354	H-28	0.199368	H-28	0.202671
H-29	0.136942	H-29	0.165680	H-29	0.164000	H-29	0.241514
H-30	0.156492	H-30	0.132973	H-30	0.171107	H-30	0.144382
H-31	0.256758	H-31	0.203500	H-31	0.197519	H-31	0.181830
H-32	0.253485	H-32	0.193186	H-32	0.114975	H-32	0.166625
H-33	0.196087	H-33	0.251664	H-33	0.152131	H-33	0.128124
N-34	−0.243941	N-34	−0.235905	H-34	0.185726	H-34	0.179658
O-35	−0.004043	O-35	0.019690	H-35	0.182535	O-35	−0.225554
O-36	0.004856	O-36	0.010521	H-36	0.241816	H-36	0.266016
H-37	0.180713	H-37	0.251873	H-37	0.227196	C-37	0.121869
Cl-38	0.438589	C-38	−0.013044	Cl-38	0.430822	H-38	0.191083
C-39	−0.011488	C-39	0.195209	C-39	0.104876	Cl-39	0.420906
H-40	0.196967	Cl-40	0.428578	H-40	0.199660		

the potential existence of electron depletion zones. Conversely, larger LOL values, signifying heightened electron localization, are evident in the inner surface regions, notably around hydrogen atoms, depicted in red, emphasizing the impact of electron localization in these regions. Overall, the ELF and LOL analyses provide comprehensive information about electron distribution and bonding characteristics within the molecule, aiding in a deeper understanding of its structural properties.[75,76]

3.3.5. QTAIM analysis. The Quantum Theory of Atoms in Molecules (QTAIM) analysis is a potent computational chemistry tool designed to explore non-covalent interactions (NCI) in molecular systems. Built upon electron density principles, the RDG analysis method utilizes this data to craft detailed 3D isosurfaces and scatter plots, unveiling the spatial distribution and intensity of weak interactions, employing color-coded graphs to distinguish interaction types, intricately depict robust interactions in blue (typically hydrogen bonding) and weaker interactions in green (resembling van der Waals forces), while red highlights regions affected by steric hindrance effects.[68,77] In this investigation, the utilization of QTAIM molecular graph analysis facilitated the exploration and visualization of NCI. The examined compounds displayed a range of intra-molecular interactions, notably van der Waals interactions indicated by (H…C) connections, characterized by sign $(\lambda 2)\rho$ values below −0.01 a.u. Moreover, (O….H) connections were identified in **4c** (ortho-NO_2) and **4d** (ortho-OH), with **4b** showcasing a distinct (Cl….H) connection. These interactions, identified *via* critical points (CPs) and intra-molecular hydrogen bond interactions highlighted by green bonds between specific atom pairs like N⋯H and O⋯H, significantly influence the stability and physical properties of the compounds. The presence of red coloration at the cores of phenyl, imidazole, and pyridine rings implies strong steric repulsion, evident from the peak presence at positive sign $(\lambda 2)\rho$ values exceeding 0.02 a.u. (Fig. 9).[63,78]

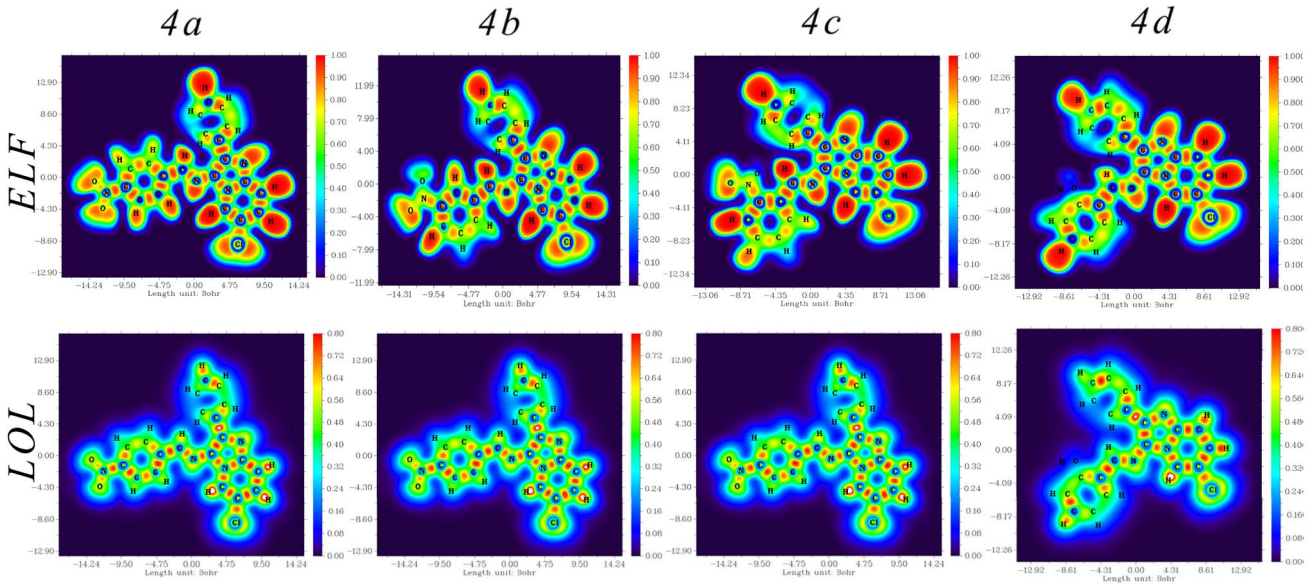

Fig. 8 ELF and LOL maps of **4a–d**.

3.4. *In vitro* anti-HIV assays

Compounds **4a–d** were assessed for their ability to inhibit HIV-1 (strain III_B) and HIV-2 (strain ROD), with monitoring of the virus-induced cytopathic effects in MT-4 cells using the MTT method. The results are presented in Table 6, where Didanosine and Nevirapine were used as positive drugs. The cytotoxicity of the compounds in MT-4 cells was also evaluated alongside their antiviral activity.

All the compounds lacked significant activity and demonstrated limited *in vitro* efficacy against HIV-1 and HIV-2 compared to the standard anti-HIV drugs. Compound **4a** displayed an EC_{50} values of 82.02 and 47.72 μg ml^{-1} against HIV-1 and HIV-2. Respectively, while **4d** was inactive at concentrations below 17.91 μg ml^{-1}.

Due to the ease of synthetic accessibility and structural modifications, these findings provide a preliminary basis for

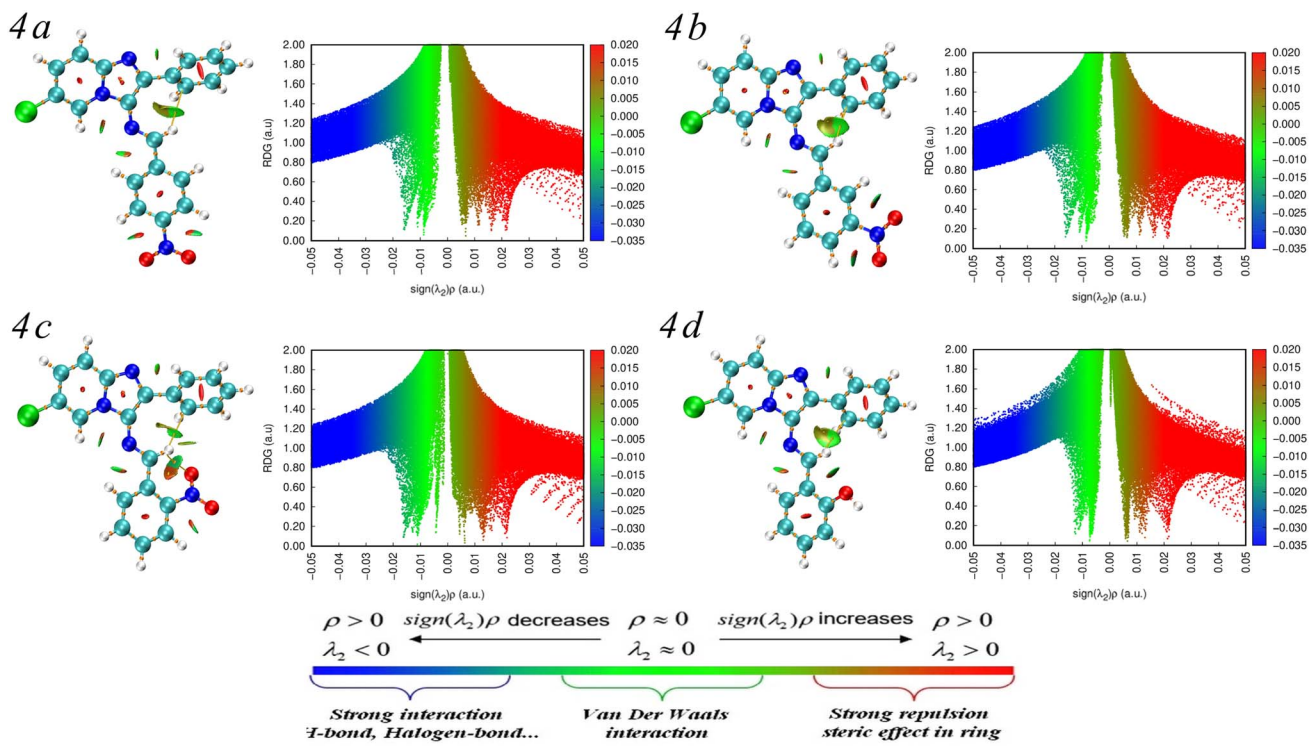

Fig. 9 NCI and RDG plot of **4a–d**.

Table 6 *In vitro* anti-HIV-1[a] and HIV-2[b] activity of **4a-d**

Compound	Virus strain	av. EC_{50}[c] (μg ml^{-1})	av. CC_{50}[d] (μg ml^{-1})	SI[e]
4a	III_B	82.02	>125.00	>2
	ROD	47.72	>125.00	>3
4b	III_B	>82.11	82.11	<1
	ROD	>82.11	82.11	<1
4c	III_B	>125.00	>125.00	X1
	ROD	>125.00	>125.00	X1
4d	III_B	>17.91	17.91	<1
	ROD	>17.91	17.91	<1
Didanosine	III_B	2.89	>50	>17
	ROD	3.39	>50	>15
Nevirapine	III_B	0.08	>4	>48
	ROD	>4.00	>4	X1

[a] Anti-HIV-1 activity measured against strain III_B. [b] Anti-HIV-2 activity measured against strain ROD. [c] Compound dose required to achieve 50% protection of MT-4 cells from HIV-1 and HIV-2-induced cytopathogenic effects. [d] Compound dose that reduces the viability of mock-infected MT-4 cells by 50%. [e] Selectivity index (SI) (CC_{50}/EC_{50}). SI value: X1 stand for 1 or <1. Values were averaged from at least three independent experiments.

further exploration, with the potential to refine these compounds for future anti-HIV applications. However, despite the limited *in vitro* activity, molecular docking and ADME studies were conducted to gain insights from both *in vitro* and *in silico* analyses.

3.5. Molecular docking studies

In this study, molecular docking simulations were conducted to assess the binding affinities of newly synthesized compounds against the HIV-1 Reverse Transcriptase (PDB ID: 1REV). The choice of HIV-1 Reverse Transcriptase as the target receptor was driven by its critical role in the HIV replication cycle, where it facilitates the conversion of viral RNA into DNA for viral integration into the host genome.[79] This enzyme is a well-established target in antiviral drug development, making it a suitable model for evaluating the potential inhibitory effects of new compounds.[80] The docking results revealed promising binding affinities for all compounds (Table 7), with docking scores of −9.8 kcal mol^{-1} for **4a**, −11.7 kcal mol^{-1} for **4b**, −11.2 kcal mol^{-1} for **4c**, and −12.7 kcal mol^{-1} for **4d**. When compared to the control molecules, Nevirapine[81] and Didanosine,[82] which displayed docking scores of −9.5 kcal mol^{-1} and −8.0 kcal mol^{-1} respectively, it is evident that the synthesized compounds exhibit superior binding potential, particularly compound **4d**, which showed the highest binding affinity. The high docking score of **4d** is particularly noteworthy because it correlates with the relatively better *in vitro* activity observed for this compound. Although the *in vitro* results for **4d** were not as strong as those for the reference drugs, **4d** showed a somewhat effective interaction with HIV-1 Reverse Transcriptase, with an EC_{50} value of >17.91 μg ml^{-1}. This suggests that the strong *in silico* binding affinity may indeed translate into some level of biological activity. The observed moderate *in vitro* efficacy of **4d**, despite its high docking score, highlights the complexity of drug interactions within a biological system. While the docking simulations predict strong binding based on static protein models,[83,84] they do not account for the dynamic and multifaceted nature of protein–ligand interactions *in vivo*.[85] Factors such as protein conformational flexibility,[86] compound solubility,[87] and stability in the biological environment[86,88] can significantly influence the actual inhibitory potential of a compound.

Table 7 Docking scores of **4a–d** against 1REV receptor with control drugs

Compound	Docking score (kcal mol^{-1})
4a	−9.8
4b	−11.7
4c	−11.2
4d	−12.7
Nevirapine	−9.5
Didanosine	−8

3.6. Molecular interactions analysis

The interaction analysis of **4a–d** against HIV-1 Reverse Transcriptase (PDB ID: 1REV) reveals crucial insights into how these molecules engage with the enzyme's active site. Each compound demonstrates a unique interaction profile, which is likely to influence its binding affinity and potential inhibitory activity. Starting with **4a** (Fig. 10a), the interaction diagram highlights significant Pi-alkyl interactions with residues such as VAL A:106, LEU A:100, and LYS A:101. These interactions contribute to the stabilization of the compound within the enzyme's hydrophobic pockets,[89,90] suggesting effective binding to the active site. Additionally, **4a** exhibits a Pi-cation interaction with LYS A:103 and a Pi-anion interaction with GLU B:138, which further stabilize its binding. These interactions align with its docking score of −9.8 kcal mol^{-1}. However, despite these promising interactions, the *in vitro* activity of **4a** was not as strong, indicating potential issues such as poor solubility or inadequate membrane permeability that might prevent the compound from achieving effective concentrations in a biological environment.

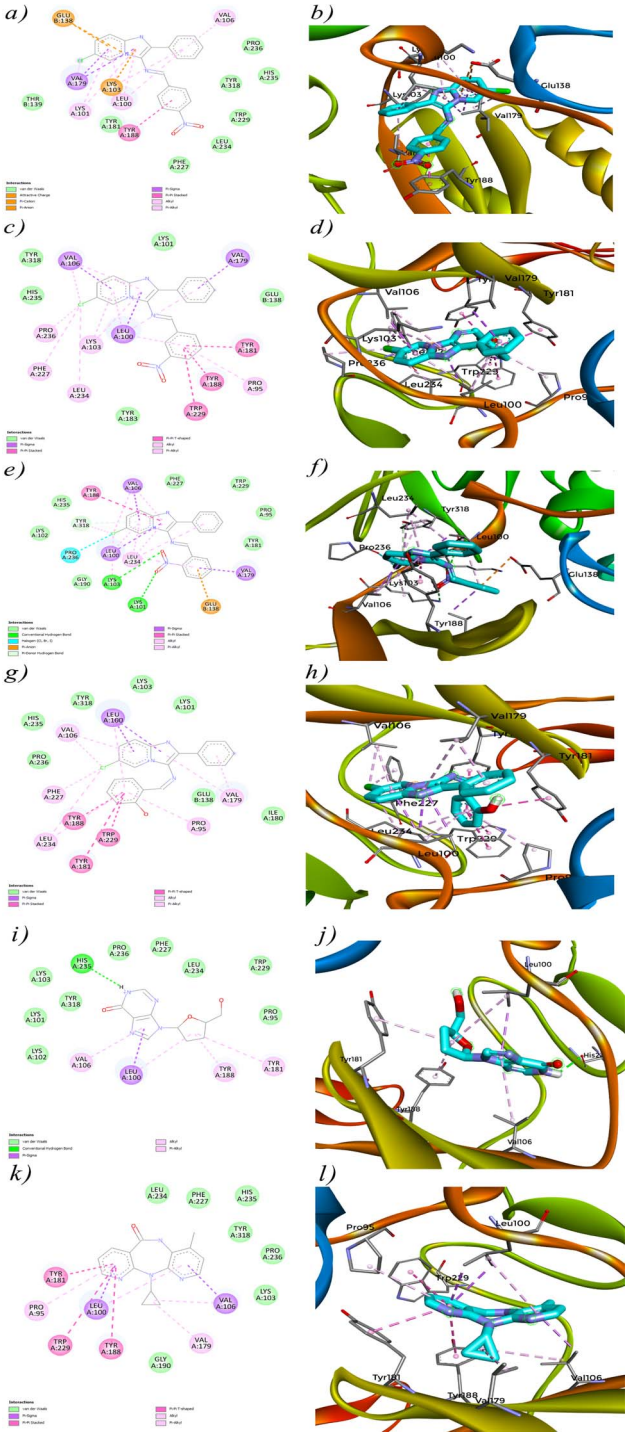

Fig. 10 2D and 3D view of interaction between compounds (**4a–d**), control drugs and protein (PDB ID: 1REV).

4b (Fig. 10c) shows an even stronger interaction profile, characterized by multiple Pi–Pi stacked and Pi–Pi T shaped interactions. Notably, residues such as TYR A:181, TRP A:229, and TYR A:181 are involved in these interactions, which are crucial for stabilizing the ligand within the active site.[91] The Pi–Pi stacked interactions, in particular, are significant for stabilizing aromatic rings within the enzyme's active site.[92] The presence of additional Pi-sigma interactions with LEU A:100, VAL A:106 and VAL A:179 enhances the binding strength of **4b**, correlating with its high docking score of −11.7 kcal mol^{-1}. However, similar to **4a**, the lack of significant *in vitro* efficacy may be due to factors like protein flexibility in a living system or the compound's pharmacokinetic properties that were not accounted for in the docking simulations. **4c** (Fig. 10e) presents a combination of Pi–Pi stacked, Pi-alkyl and conventional hydrogen bond interactions. The compound engages in strong Pi–Pi stacked and Pi-aninon interactions with TYR A:188 and GLU B:138, helping anchor it within the active site. Hydrogen bonding with LYS A:101 and LYS A:103 suggests that **4c** also engages in traditional polar interactions, contributing to its binding affinity. Despite these interactions, the docking score of −11.2 kcal mol^{-1} for **4c** is slightly lower than that of **4b**, which might indicate a less optimal binding orientation or fewer critical contacts within the active site. The moderate *in vitro* performance of **4c** could stem from similar factors that affected **4a** and **4b**, such as solubility issues or the dynamic nature of the protein–ligand interactions in a biological context. **4d** (Fig. 10g) stands out with the strongest interaction profile among the synthesized compounds, consistent with its highest docking score of −12.7 kcal mol^{-1}. The compound forms extensive Pi–Pi stacked, T shaped and Pi-alkyl interactions with multiple key residues, including TYR A:188, TRP A:229, TYR A:181, PRO A:95 and VAL A:106. The significant Pi-sigma interaction with LEU A:100 likely enhances the electrostatic stability of **4d** within the binding site. The variety and density of these interactions suggest that **4d** is highly effective at engaging the active site of HIV-1 Reverse Transcriptase, contributing to its superior binding affinity. This extensive interaction profile is similar to that observed for the reference molecule Nevirapine, which also relies on strong hydrophobic and electrostatic interactions within the active site. The promising *in vitro* activity of **4d**, albeit not as strong as Nevirapine, reinforces its potential as a candidate for further development, particularly because its interaction profile closely resembles that of the control molecule. The comparison between the synthesized compounds and the reference molecules, Didanosine (Fig. 10i) and Nevirapine (Fig. 10k), highlights the superior interaction profiles of the synthesized compounds, especially **4d**. Nevirapine primarily relies on Pi-alkyl, Pi-sigma and Pi–Pi stacked/T shaped interactions with key residues like PRO A:95, TYR A:181, TYR A:188, LEU A:100 and VAL A:106, while Didanosine, despite its lower docking score, forms conventional hydrogen bonds and Pi-sigma interactions that are less extensive than those observed for the synthesized compounds. However, the lack of significant *in vitro* efficacy for most of these compounds, despite strong docking scores, suggests a non-correlation between the *in silico* predictions and actual biological activity. One possible hypothesis for this discrepancy is that docking simulations, which typically involve static models of the protein, may not fully capture the dynamic nature of proteins *in vivo*. Additionally, factors such as poor solubility, inadequate membrane permeability, or compound instability in biological conditions could have prevented these compounds from achieving effective concentrations at the target site, leading to reduce *in vitro* efficacy.

3.7. *In silico* prediction of ADME properties

The ADME analysis of **4a–d** alongside the control molecules provides critical insights into their drug-likeness (Table 8) and pharmacokinetic profiles (Table 9).[55] These properties are essential for understanding how these compounds might behave in a biological system, particularly with regard to their solubility, absorption, distribution, and potential metabolic interactions.[93] Starting with solubility, which is a key factor influencing the bioavailability of a drug,[87,94] the synthesized compounds show varying levels of solubility. Compounds **4a**, **4b**, and **4c** all fall into the "poorly soluble" category, with Log *S* values of −6.85. Poor solubility can significantly limit the effectiveness of a drug, as it may hinder the compound's ability to dissolve in the biological fluids and reach sufficient concentrations at the target site. This limitation is likely a contributing factor to the less promising *in vitro* results observed for these compounds, despite their high docking scores. In contrast, compound **4d** stands out with a Log *S* value of −5.78, placing it in the "moderately soluble" category. This enhanced solubility compared to the other synthesized compounds suggests that **4d** may have a better chance of achieving effective concentrations *in vivo*, which could partially explain its relatively better *in vitro* activity. The moderately soluble nature of **4d**, coupled with its strong docking interactions, makes it a promising candidate for further development. Additionally, **4d** shows an advantage in permeability, being BBB permeant, which could potentially make it more effective in crossing biological barriers to reach the target site. When comparing the synthesized compounds to the control molecules, Nevirapine and Didanosine demonstrate superior solubility with Log *S* values of −2.92 and 0.02, respectively, classifying them as "soluble" and "highly soluble." These solubility profiles are indicative of their well-established efficacy in clinical use, as higher solubility typically correlates with better absorption and bioavailability.[95] Nevirapine's ability to be BBB permeant[96] further enhances its pharmacokinetic profile, ensuring it can reach its target effectively. Didanosine, although not BBB permeant, benefits from its excellent solubility, which facilitates its distribution and action within the body. Beyond solubility, the ADME analysis also highlights other important factors such as lipophilicity (XlogP3),[97] gastrointestinal absorption,[98] and potential interactions with metabolic enzymes.[99] All the synthesized compounds, including **4d**, have high lipophilicity (XlogP3 > 5 for **4a**, **4b**, and **4c**; 5.33 for **4d**), which is generally favorable for membrane permeability but can sometimes lead to issues such as poor solubility or increased potential for off–target interactions. The control molecules, Nevirapine and Didanosine, exhibit lower lipophilicity, which, combined with their superior solubility, likely contributes to their well-balanced pharmacokinetic profiles. In terms of gastrointestinal absorption, all compounds, including the synthesized ones, are predicted to have high GI absorption, which is advantageous for oral administration. Finally, the absence of alerts in the PAINS filter across all compounds suggests that they are unlikely to interfere with or generate false-positive results in biological assays,[100] further supporting their suitability for drug development. In summary, while the synthesized compounds show limitations due to poor solubility, **4d** emerges as a more promising candidate due to its moderate solubility, high permeability, and strong docking interactions. The superior solubility and pharmacokinetic profiles of the control molecules, Nevirapine and Didanosine, underscore the importance of optimizing solubility and other ADME properties in the development of new antiviral agents. Further optimization of **4d**'s properties, particularly in improving its solubility and ensuring effective *in vivo* performance, could enhance its potential as a therapeutic agent.

3.8. Aqueous solubility

Aqueous solubility is a critical factor that influences a drug's absorption, distribution, metabolism, and excretion properties *in vivo*. It is well-established that poor water solubility can result

Table 8 Lipinski's rule of five **4a–d** with control drugs

Compound	Lipinski's rule	H-bond acceptors	H-bond donors	Molecular weight	MLOGP
4a	YES	4	0	376.8	4.12
4b	YES	4	0	376.8	4.12
4c	YES	4	0	376.8	4.12
4d	YES	3	1	347.8	3.39
Nevirapine	YES	3	1	266.3	2.14
Didanosine	YES	5	2	236.23	−0.2

Table 9 ADME properties of **4a–d** along with control drugs

Compound	XlogP3	Log *S*	Solubility class	GIA	BBB	P-gp	CYP2D6 inhibitor	CYP3A4 inhibitor	PAINS alert
4a	5.51	−6.85	Poorly soluble	High	No	No	No	No	0 Alert
4b	5.51	−6.85	Poorly soluble	High	No	No	No	No	0 Alert
4c	5.51	−6.85	Poorly soluble	High	No	No	No	No	0 Alert
4d	5.33	−5.78	Moderately soluble	High	Yes	No	Yes	No	0 Alert
Nevirapine	1.96	−2.92	Soluble	High	Yes	Yes	No	No	0 Alert
Didanosine	−1.47	0.02	Highly soluble	High	No	No	No	No	0 Alert

Table 10 Aqueous solubility of **4a–d** at pH = 7.0

Compound	4a	4b	4c	4d
Solubility (μg mL^{-1})	25	25	<1	125

in unfavorable pharmacokinetic profiles, such as low oral bioavailability and a short half-life, ultimately limiting a drug's therapeutic efficacy.[101,102] Therefore, assessing the solubility of drug candidates has become essential in optimizing their pharmacological potential.

The aqueous solubility of the synthesized imidazopyridine-Schiff base derivatives was evaluated at pH 7.0 to understand its impact on their observed anti-HIV activity. The solubility data presented in Table 10 indicate a noticeable correlation with antiviral efficacy. Compound **4d**, which exhibited the highest solubility (125 μg ml^{-1}), demonstrated relatively better antiviral activity, with EC_{50} values of 17.91 μg ml^{-1}. This suggests that enhanced solubility may facilitate better interaction with viral targets, leading to improved activity. Compounds **4a** and **4b**, with moderate solubility (25 μg ml^{-1}), showed limited antiviral effects, for instance, compound **4a** achieved an EC_{50} of 82.02 μg ml^{-1} against HIV-1 and 47.72 μg ml^{-1} against HIV-2. In contrast, compound **4c**, which had very low solubility (<1 μg ml^{-1}), showed no anti-HIV activity, with EC_{50} values exceeding 125 μg ml^{-1} for both viral strains. These observations suggest that solubility plays a crucial role in the bioavailability and antiviral performance of the compounds. Therefore, optimizing aqueous solubility could be a key factor in enhancing the antiviral potential of future derivatives.

4. Conclusion

In this study, new imidazo[1,2-*a*]pyridine-Schiff base derivatives were synthesized and characterized using various spectroscopic techniques, with the structure of compound **4a** further confirmed by single-crystal X-ray diffraction analysis. Additionally, DFT calculations were employed to explore the electronic and structural properties of the compounds, providing valuable insights into their potential reactivity and interaction with biological targets. The *in vitro* antiviral evaluation against HIV-1 and HIV-2 revealed limited efficacy compared to standard anti-HIV drugs. Despite this, molecular docking analyses demonstrated notable binding affinities for HIV-1 reverse transcriptase, surpassing those of the reference drugs. However, the promising docking results did not translate into significant *in vitro* activity, likely due to poor solubility and suboptimal pharmacokinetic properties, as suggested by ADME analysis and aqueous solubility. Consequently, further structural optimization, particularly focusing on improving solubility and bioavailability, is essential to enhance the therapeutic potential of these compounds.

Data availability

The data supporting this article have been included as part of the ESI.† Crystallographic data for compound **4a** has been deposited at the Cambridge Crystallographic Data Centre (CCDC) under deposition Number 2391520 and can be obtained from https://www.ccdc.cam.ac.uk/structures/Search?ccdc=2391520.

Author contributions

Mohamed Azzouzi: validation, writing – original draft. Abderrahim Ait Ouchaoui: investigation, methodology. Omar Azougagh: software, formal analysis. Salah Eddine El Hadad: software, methodology. Mohamed Abou-salama: resources, formal analysis. Adyl Oussaid: data curation, methodology. Christophe Pannecouque: methodology, investigation, validation, reviewing and editing. Taoufik Rohand: validation, supervision.

Conflicts of interest

The authors declare that they have no known competing financial interests or personal relationships that could have appeared to influence the work reported in this paper.

Acknowledgements

The authors thank their respective institutions for providing the necessary facility to complete this work.

References

1 P. N. Kalaria, S. C. Karad and D. K. Raval, *Eur. J. Med. Chem.*, 2018, **158**, 917–936.
2 B. Zhang and A. Studer, *Chem. Soc. Rev.*, 2015, **44**, 3505–3521.
3 B. R. Smith, C. M. Eastman and J. T. Njardarson, *J. Med. Chem.*, 2014, **57**, 9764–9773.
4 W.-Y. Fang, L. Ravindar, K. P. Rakesh, H. M. Manukumar, C. S. Shantharam, N. S. Alharbi and H.-L. Qin, *Eur. J. Med. Chem.*, 2019, **173**, 117–153.
5 B. Narasimhan, D. Sharma and P. Kumar, *Med. Chem. Res.*, 2011, **20**, 1119–1140.
6 A. K. Bagdi, S. Santra, K. Monir and A. Hajra, *Chem. Commun.*, 2015, **51**, 1555–1575.
7 K. Pericherla, P. Kaswan, K. Pandey and A. Kumar, *Synthesis*, 2015, **47**, 887–912.
8 R. Goel, V. Luxami and K. Paul, *RSC Adv.*, 2015, **5**, 81608–81637.
9 C. Enguehard-Gueiffier and A. Gueiffier, *Mini-Rev. Med. Chem.*, 2007, **7**, 888–899.
10 M. H. Fisher and A. Lusi, *J. Med. Chem.*, 1972, **15**, 982–985.
11 Y. Rival, G. GRASSY and G. MICHEL, *Chem. Pharm. Bull.*, 1992, **40**, 1170–1176.
12 A. Nordqvist, M. T. Nilsson, O. Lagerlund, D. Muthas, J. Gising, S. Yahiaoui, L. R. Odell, B. R. Srinivasa, M. Larhed, S. L. Mowbray and A. Karlén, *MedChemComm*, 2012, **3**, 620–626.
13 T. H. Al-Tel and R. A. Al-Qawasmeh, *Eur. J. Med. Chem.*, 2010, **45**, 5848–5855.

14 G. C. Moraski, L. D. Markley, P. A. Hipskind, H. Boshoff, S. Cho, S. G. Franzblau and M. J. Miller, *ACS Med. Chem. Lett.*, 2011, **2**, 466–470.
15 S. Kumar, N. Sharma, I. K. Maurya, A. K. K. Bhasin, N. Wangoo, P. Brandão, V. Félix, K. K. Bhasin and R. K. Sharma, *Eur. J. Med. Chem.*, 2016, **123**, 916–924.
16 N. P. Mishra, S. Mohapatra, C. R. Sahoo, B. P. Raiguru, S. Nayak, S. Jena and R. N. Padhy, *J. Mol. Struct.*, 2021, **1246**, 131183.
17 C. Wei, J. Huang, Y. Luo, S. Wang, S. Wu, Z. Xing and J. Chen, *Pestic. Biochem. Physiol.*, 2021, **175**, 104857.
18 G. Puerstinger, J. Paeshuyse, E. De Clercq and J. Neyts, *Bioorg. Med. Chem. Lett.*, 2007, **17**, 390–393.
19 C. Li, R. Song, S. He, S. Wu, S. Wu, Z. Wu, D. Hu and B. Song, *J. Agric. Food Chem.*, 2022, **70**, 7375–7386.
20 J.-M. Chezal, J. Paeshuyse, V. Gaumet, D. Canitrot, A. Maisonial, C. Lartigue, A. Gueiffier, E. Moreau, J.-C. Teulade, O. Chavignon and J. Neyts, *Eur. J. Med. Chem.*, 2010, **45**, 2044–2047.
21 N. Dahan-Farkas, C. Langley, A. L. Rousseau, D. B. Yadav, H. Davids and C. B. de Koning, *Eur. J. Med. Chem.*, 2011, **46**, 4573–4583.
22 N. Masurier, E. Debiton, A. Jacquemet, A. Bussière, J.-M. Chezal, A. Ollivier, D. Tétégan, M. Andaloussi, M.-J. Galmier, J. Lacroix, D. Canitrot, J.-C. Teulade, R. C. Gaudreault, O. Chavignon and E. Moreau, *Eur. J. Med. Chem.*, 2012, **52**, 137–150.
23 J. Dam, Z. Ismail, T. Kurebwa, N. Gangat, L. Harmse, H. M. Marques, A. Lemmerer, M. L. Bode and C. B. de Koning, *Eur. J. Med. Chem.*, 2017, **126**, 353–368.
24 S. Endoori, K. C. Gulipalli, S. Bodige, P. Ravula and N. Seelam, *J. Heterocycl. Chem.*, 2021, **58**, 1311–1320.
25 M. Reddy Gangireddy, M. Mantipally, R. Gundla, V. Nayak Badavath, K. Paidikondala and A. Yamala, *ChemistrySelect*, 2019, **4**, 13622–13629.
26 M. Hieke, C. B. Rödl, J. M. Wisniewska, E. la Buscató, H. Stark, M. Schubert-Zsilavecz, D. Steinhilber, B. Hofmann and E. Proschak, *Bioorg. Med. Chem. Lett.*, 2012, **22**, 1969–1975.
27 J. I. Serrano-Contreras, M. E. Meléndez-Camargo, Y. K. Márquez-Flores, M. P. Soria-Serrano and M. E. Campos-Aldrete, *Toxicol. Res.*, 2022, **11**, 730–742.
28 A. L. Berhanu, Gaurav, I. Mohiuddin, A. K. Malik, J. S. Aulakh, V. Kumar and K.-H. Kim, *TrAC, Trends Anal. Chem.*, 2019, **116**, 74–91.
29 M. N. Uddin, S. S. Ahmed and S. M. R. Alam, *J. Coord. Chem.*, 2020, **73**, 3109–3149.
30 C. Verma and M. A. Quraishi, *Coord. Chem. Rev.*, 2021, **446**, 214105.
31 B. D. Nath, M. M. Islam, M. R. Karim, S. Rahman, M. A. A. Shaikh, P. E. Georghiou and M. Menelaou, *ChemistrySelect*, 2022, **7**, 202104290.
32 A. Kajal, S. Bala, S. Kamboj, N. Sharma and V. Saini, *J. Catal.*, 2013, **2013**, 893512.
33 A. Hamad, Y. Chen, M. A. Khan, S. Jamshidi, N. Saeed, M. Clifford, C. Hind, J. M. Sutton and K. M. Rahman, *MicrobiologyOpen*, 2021, **10**, 1218.
34 L. Wei, J. Zhang, W. Tan, G. Wang, Q. Li, F. Dong and Z. Guo, *Int. J. Biol. Macromol.*, 2021, **179**, 292–298.
35 C. M. da Silva, D. L. da Silva, L. V. Modolo, R. B. Alves, M. A. de Resende, C. V. B. Martins and Â. de Fátima, *J. Adv. Res.*, 2011, **2**, 1–8.
36 M. S. Tople, N. B. Patel, P. P. Patel, A. C. Purohit, I. Ahmad and H. Patel, *J. Mol. Struct.*, 2023, **1271**, 134016.
37 N. Uddin, F. Rashid, S. Ali, S. A. Tirmizi, I. Ahmad, S. Zaib, M. Zubair, P. L. Diaconescu, M. N. Tahir, J. Iqbal and A. Haider, *J. Biomol. Struct. Dyn.*, 2020, **38**, 3246–3259.
38 S. Shekhar, A. M. Khan, S. Sharma, B. Sharma and A. Sarkar, *Emergent Mater.*, 2022, **5**, 279–293.
39 S. Kaushik, S. K. Paliwal, M. R. Iyer and V. M. Patil, *Med. Chem. Res.*, 2023, **32**, 1063–1076.
40 R. Cordeiro and M. Kachroo, *Bioorg. Med. Chem. Lett.*, 2020, **30**, 127655.
41 N. Yuldasheva, N. Acikyildiz, M. Akyuz, L. Yabo-Dambagi, T. Aydin, A. Cakir and C. Kazaz, *J. Mol. Struct.*, 2022, **1270**, 133883.
42 Z. Wang, Z. Yu, D. Kang, J. Zhang, Y. Tian, D. Daelemans, E. De Clercq, C. Pannecouque, P. Zhan and X. Liu, *Bioorg. Med. Chem.*, 2019, **27**, 447–456.
43 S. Xu, L. Sun, A. Dick, W. A. Zalloum, T. Huang, M. E. Meuser, X. Zhang, Y. Tao, S. Cherukupalli, D. Ding, X. Ding, S. Gao, X. Jiang, D. Kang, E. De Clercq, C. Pannecouque, S. Cocklin, X. Liu and P. Zhan, *Eur. J. Med. Chem.*, 2022, **227**, 113903.
44 D. M. Margolis and D. J. Hazuda, *Curr. Opin. HIV AIDS*, 2013, **8**, 230–235.
45 D. Kang, Z. Huo, G. Wu, J. Xu, P. Zhan and X. Liu, *Expert Opin. Ther. Pat.*, 2017, **27**, 383–391.
46 L. Sun, T. Huang, A. Dick, M. E. Meuser, W. A. Zalloum, C.-H. Chen, X. Ding, P. Gao, S. Cocklin, K.-H. Lee, P. Zhan and X. Liu, *Eur. J. Med. Chem.*, 2020, **190**, 112085.
47 M. Azzouzi, O. Azougagh, A. A. Ouchaoui, S. e. El hadad, S. Mazières, S. E. Barkany, M. Abboud and A. Oussaid, *ACS Omega*, 2024, **9**, 837–857.
48 C. Pannecouque, D. Daelemans and E. De Clercq, *Nat. Protoc.*, 2008, **3**, 427–434.
49 H. M. Berman, J. Westbrook, Z. Feng, G. Gilliland, T. N. Bhat, H. Weissig, I. N. Shindyalov and P. E. Bourne, *Nucleic Acids Res.*, 2000, **28**, 235–242.
50 G. M. Morris, R. Huey, W. Lindstrom, M. F. Sanner, R. K. Belew, D. S. Goodsell and A. J. Olson, *J. Comput. Chem.*, 2009, **30**, 2785–2791.
51 N. M. O'Boyle, M. Banck, C. A. James, C. Morley, T. Vandermeersch and G. R. Hutchison, *J. Cheminf.*, 2011, **3**, 33.
52 S. Kim, P. A. Thiessen, E. E. Bolton, J. Chen, G. Fu, A. Gindulyte, L. Han, J. He, S. He, B. A. Shoemaker, J. Wang, B. Yu, J. Zhang and S. H. Bryant, *Nucleic Acids Res.*, 2015, **44**, 1202–1213.
53 O. Trott and A. J. Olson, *J. Comput. Chem.*, 2010, **31**, 455–461.
54 U. Baroroh, M. Biotek, Z. S. Muscifa, W. Destiarani, F. G. Rohmatullah and M. Yusuf, *Indonesian Journal of Computational Biology*, 2023, **2**, 22–30.

55 A. Daina, O. Michielin and V. Zoete, *Sci. Rep.*, 2017, **7**, 42717.
56 G. Vijayakumari, N. Iyandurai, M. Raja, V. Vetrivelan, A. Thamarai, S. Javed and S. Muthu, *Chem. Phys. Impact*, 2023, **6**, 100190.
57 J. Yu, N. Q. Su and W. Yang, *JACS Au*, 2022, **2**, 1383–1394.
58 H. M. Abd El-Lateef, M. M. Khalaf, A. A. Amer, M. Kandeel, A. A. Abdelhamid and A. Abdou, *ACS Omega*, 2023, **8**, 25877–25891.
59 J. S. Al-Otaibi, Z. Ullah, Y. S. Mary, Y. S. Mary, S. Soman, M. Thirunavukkarasu and H. W. Kwon, *Vietnam J. Chem.*, 2022, **60**, 636–652.
60 S. M. Al-Muntaser, A. A. Al-Karmalawy, A. M. El-Naggar, A. K. Ali, N. E. A. Abd El-Sattar and E. M. Abbass, *RSC Adv.*, 2023, **13**, 12184–12203.
61 F. Rizwana B, S. Muthu, J. C. Prasana, C. S. Abraham and M. Raja, *Chem. Data Collect.*, 2018, **17–18**, 236–250.
62 J. D. D. Tarika, X. D. D. Dexlin, S. Madhankumar, D. D. Jayanthi and T. J. Beaula, *Spectrochim. Acta, Part A*, 2021, **259**, 119907.
63 V. Puthanveedu and K. Muraleedharan, *Comput. Theor. Chem.*, 2023, **1225**, 114126.
64 G. Jeyanthi and C. Gnana Sambandam, *J. Mol. Struct.*, 2021, **1243**, 130879.
65 S. Janani, H. Rajagopal, S. Sakthivel, S. Kadaikunnan, G. Abbas and S. Muthu, *J. Mol. Struct.*, 2023, **1289**, 135832.
66 Y. Kubota, S. Tanaka, K. Funabiki and M. Matsui, *Org. Lett.*, 2012, **14**, 4682–4685.
67 D. S. El Sayed and E.-s. M. Abdelrehim, *Spectrochim. Acta, Part A*, 2021, **261**, 120006.
68 O. Azougagh, S. Essayeh, N. Achalhi, A. El Idrissi, H. Amhamdi, M. Loutou, Y. El Ouardi, A. Salhi, M. Abou-Salama and S. El Barkany, *Carbohydr. Polym.*, 2022, **276**, 118737.
69 A. Prabakaran, V. Vijayakumar, N. Radhakrishnan, R. Chidambaram and S. Muthu, *Polycyclic Aromat. Compd.*, 2022, **42**, 925–941.
70 I. Azad, Y. Akhter, T. Khan, M. I. Azad, S. Chandra, P. Singh, D. Kumar and M. Nasibullah, *J. Mol. Struct.*, 2020, **1203**, 127285.
71 A. Jeelani, S. Muthu, B. R. Raajaraman and S. Sevvanthi, *Spectrosc. Lett.*, 2020, **53**, 778–792.
72 J. Geethapriya, A. Shanthidevi, M. Arivazhagan, N. Elangovan and R. Thomas, *J. Indian Chem. Soc.*, 2022, **99**, 100418.
73 S. Sundaram, V. N. Vijayakumar and V. Balasubramanian, *Comput. Theor. Chem.*, 2022, **1217**, 113920.
74 S. Sevvanthi, S. Muthu, S. Aayisha, P. Ramesh and M. Raja, *Chem. Data Collect.*, 2020, **30**, 100574.
75 K. Arulaabaranam, G. Mani and S. Muthu, *Chem. Data Collect.*, 2020, **29**, 100525.
76 S. Janani, H. Rajagopal, S. Muthu, S. Javed and A. Irfan, *J. Indian Chem. Soc.*, 2022, **99**, 100438.
77 M. Azzouzi, Z. E. Ouafi, O. Azougagh, W. Daoudi, H. Ghazal, S. E. Barkany, R. Abderrazak, S. Mazières, A. E. Aatiaoui and A. Oussaid, *J. Mol. Struct.*, 2023, **1285**, 135525.
78 M. Thirunavukkarasu, P. Prabakaran, A. Saral, N. S. Alharbi, S. Kadaikunnan, A. S. Kazachenko and S. Muthu, *J. Mol. Liq.*, 2023, **380**, 121714.
79 W. S. Hu and S. H. Hughes, *Cold Spring Harbor Perspect. Med.*, 2012, **2**, a006882.
80 E. De Clercq, *J. Clin. Virol.*, 2004, **30**, 115–133.
81 A. Milinkovic and E. Martínez, *Expert Rev. Anti-Infect. Ther.*, 2004, **2**, 367–373.
82 M. J. M. Hitchcock, *Clin. Infect. Dis.*, 1993, **16**, 16–21.
83 L. G. Ferreira, R. N. Dos Santos, G. Oliva and A. D. Andricopulo, *Molecules*, 2015, **20**, 13384–13421.
84 L. Pinzi and G. Rastelli, *Int. J. Mol. Sci.*, 2019, **20**, 4331.
85 J. Wang, A. Bhattarai, H. N. Do and Y. Miao, *QRB Discovery*, 2022, **3**, 13.
86 K. Henzler-Wildman and D. Kern, *Nature*, 2007, **450**, 964–972.
87 C. A. Lipinski, F. Lombardo, B. W. Dominy and P. J. Feeney, *Adv. Drug Delivery Rev.*, 1997, **23**, 3–25.
88 J. A. McCammon, *Curr. Opin. Struct. Biol.*, 1998, **8**, 245–249.
89 R. Patil, S. Das, A. Stanley, L. Yadav, A. Sudhakar and A. K. Varma, *PLoS One*, 2010, **5**, 12029.
90 R. Vaidyanathan, S. Murugan Sreedevi, K. Ravichandran, S. M. Vinod, Y. Hari Krishnan, L. K. Babu, P. S. Parthiban, L. Basker, T. Perumal, V. Rajaraman, G. Arumugam, K. Rajendran and V. Mahalingam, *JCIS Open*, 2023, **12**, 100096.
91 J. Ribas, E. Cubero, F. J. Luque and M. Orozco, *J. Org. Chem.*, 2002, **67**, 7057–7065.
92 G. B. McGaughey, M. Gagné and A. K. Rappé, *J. Biol. Chem.*, 1998, **273**, 15458–15463.
93 F. Yamashita and M. Hashida, *Drug Metab. Pharmacokinet.*, 2004, **19**, 327–338.
94 T. J. Hou, K. Xia, W. Zhang and X. J. Xu, *J. Chem. Inf. Comput. Sci.*, 2004, **44**, 266–275.
95 A. K. Shah and S. A. Agnihotri, *J. Controlled Release*, 2011, **156**, 281–296.
96 Y. Yuan, F. Zheng and C.-G. Zhan, *AAPS J.*, 2018, **20**, 54.
97 R. Datta, D. Das and S. Das, *Chemom. Intell. Lab. Syst.*, 2021, **213**, 104309.
98 N. Basant, S. Gupta and K. P. Singh, *Comput. Biol. Chem.*, 2016, **61**, 178–196.
99 T. Lynch and A. Price, *Am. Fam. Physician*, 2007, **76**, 391–396.
100 J. B. Baell and J. W. M. Nissink, *ACS Chem. Biol.*, 2018, **13**, 36–44.
101 J.-S. Wang, K.-X. Zhao, K. Zhang, C. Pannecouque, E. De Clercq, S. Wang and F.-E. Chen, *Bioorg. Chem.*, 2024, **147**, 107340.
102 H. Chen, C. Khemtong, X. Yang, X. Chang and J. Gao, *Drug Discovery Today*, 2011, **16**, 354–360.